Extraction of Atom-Diatom Collision Properties by Least Squares Fitting

by

James Wampler

Class of 2011

Faculty Advisor: Brian Stewart

A thesis submitted to the
faculty of Wesleyan University
in partial fulfillment of the requirements for the
Degree of Bachelor of Arts
with Departmental Honors in Physics

Contents

CHAPTER 1

Introduction

In this document, we will develop a method to quickly extract two properties fundamental to collision dynamics from spectral collision data. The first property is the cross section, which we will study as a function of collision energy. The second property is the three-body potential. These are to some extent two separate projects. However, these two projects are similar and related. They relate first in their goal – to extract properties that can help give us an understanding of the collision dynamics. They relate in the least squares fitting method that we use to extract both properties.

These two properties are related in yet one more way: the three-body potential informs of the forces on the particles, which in turn informs us of the collision dynamics and even the velocity-dependent cross section. Despite this, it is still useful to fit the velocity-dependent cross section separately, as a direct fit will produce more reliable results.

These properties will be extracted from three-body collision data. Our motivation for exploring the three-body system is that it is extremely simple yet full of rich behavior and still incompletely explored. Our motivation for choosing a simple system is that in this sort of system we are more capable of extracting information that is both meaningful and fundamental to the system. More complicated systems would be difficult to study at the same level of detail. For these reasons, we choose a very simple system. In fact, the three-body system is the simplest

collisional system bar one. The most fundamental collisions are two-body collisions. However, the two-body problem was solved in the 17th century. [1] As a solved problem, the essential physics of a two-body collision is well understood and therefore is not the most interesting pursuit for further study.

The next most simple problem is the three-body problem. While this problem is seemingly not much more complicated than the two-body problem, it is enough so that with the extra body comes the onset of chaos. [2] Still, though it is not a solvable problem, we can learn quite a bit about the essential physics of the situation.

The first property – the velocity-dependent cross section – allows us to gain an understanding of the effects of varying collision energy on the collision dynamics. Chapter 3 will detail the method of extracting velocity-dependent cross sections.

The second property – the three-body potential – gives us an understanding of the collision dynamics themselves. Chapter 4 will detail the method of extracting three-body potential functions.

CHAPTER 2

Background and Motivation

In our lab we study collisions of the lithium dimer (Li_2) with a collision partner, usually a nonreactive ideal gas. In this document we will focus on collisions with neon. After initial excitation by the laser of the Li_2 ($A^1\Sigma_u^+$) system, the molecule decays back down to the ground state, emitting fluorescence. Fluorescence from molecules that collide elastically or do not collide is called parent fluorescence. If the molecule undergoes an inelastic collision, there is satellite fluorescence. [3] If the molecule undergoes a rotationally inelastic collision, Δj, the change in the rotational quantum state is always even. [4]

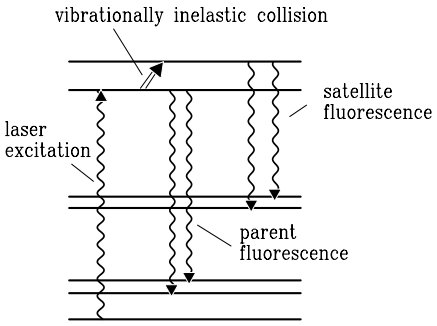

Figure 1: After excitation, inelastic collisions cause satellite fluorescence. In the absence of one, parent fluorescence is emitted. Pictured here is a vibrationally inelastic collision. Image from Stewart *et al.*, 2010 [3]

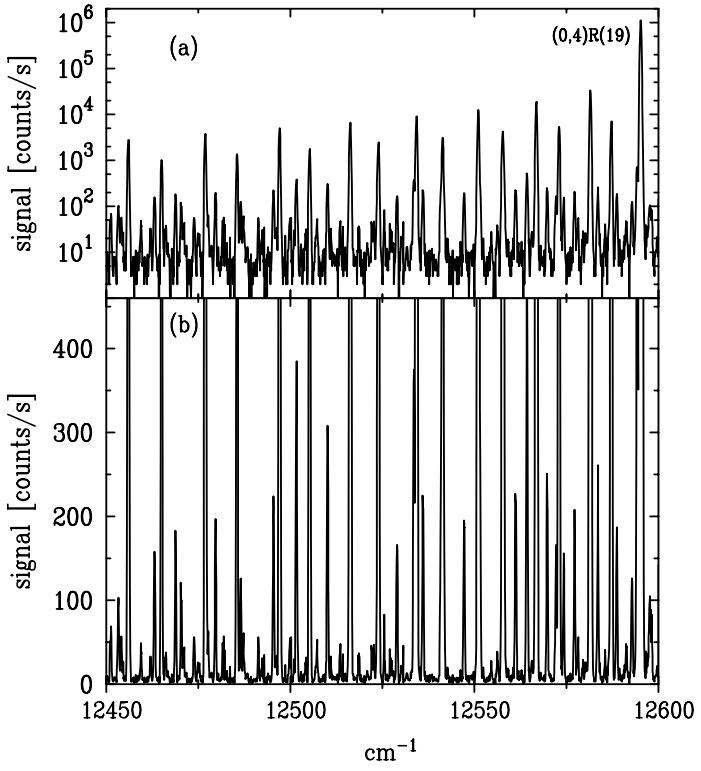

Figure 2: Part of a fluorescence spectrum. (a) Many satellite lines are visible, as is one parent line on the right side of the image. (b) Vibrationally inelastic satellite lines are smaller than rotationally inelastic lines. Image from Stewart *et al.*, 2010 [3]

As we see in figure 2, fluorescence is not emitted as a series of delta functions, but rather is emitted as a spectral line shape with finite width. The ratio of the intensity of the satellite line divided by the intensity of the parent line at any given detuning is referred to the line shape ratio of that collisionally populated state.

We can model the rate of change of the population in an excited state as

$$\frac{dn_f}{dt} = k_{if} n_i n_X - \Gamma_f n_f \tag{1}$$

Here, n_f is the population of a given collisionally populated final state, n_i is the population of the initial excited state and n_X is the population of the collision partner; Γ_f is the rate of decay from the final state f and k_{if} is the thermally averaged rate constant of the collision leading to final state f. [3]

If we assume a steady state solution, we can solve for the ratio of final state population to initial state population in terms of the rate constant and two quantities as below:

$$k_{if} = \frac{\Gamma_f n_f}{n_x n_i}. \tag{2}$$

These two quantities are n_x, the partial pressure of the collision partner and Γ_f, which has been previously measured. [5]

This ratio of excited state population to ground state population is proportional to the ratio of the magnitude of the lineshape at a given detuning. We call this quantity the line shape ratio.

In these collisions, there are two properties that we are particularly interested in. The first property is the three-body potential function around the molecules. This potential function informs us of the dynamics of the molecule of the collision partner. The second property we are interested in is the collisional cross section, which we are going to study as a function of collision energy or equivalently the

relative velocity of the molecule and the collision partner. The velocity-dependent cross section is a product of the dynamics and can give us a better understanding of the effects of relative velocity on the collision.

For a relative velocity v_r, a cross section $\sigma_{if}(v_r)$ and a velocity-dependent collisional rate constant k_{if}, we have

$$v_r \sigma_{if}(v_r) = k_{if}. \tag{3}$$

Unfortunately, this function cannot be obtained directly from the experimental data. This is because the experimental data represents collisions happening at a range of speeds and the data for individual collision energies cannot be separated. As described in chapter 3, by tuning the laser we can excite groups of molecules traveling with varying velocities in the direction of the laser, allowing us to build a relation between the velocity-dependent cross section and the detuning of the laser from resonance.

The three-body potential tells us still more about the system. By extracting the three-body potential, we could understand the full dynamics of the collision. It is possible to calculate an *ab initio* potential for a given system to get a close approximation of the actual potential. The existence of the 1991 Alexander-Werner Li_2-Ne potential surface is particularly convenient. [6] However, as a general method for discovering three-body potentials, *ab initio* calculation is insufficient. Firstly this is because *ab initio* calculations are extremely difficult to create, so unless an *ab initio* potential surface exists already, if we desire to study an arbitrary system, it is not practical for us, as experimentalists, to derive one. Secondly, while they are close approximations, *ab initio* calculations are not perfect. [7] The method developed in chapter 4 will provide a quicker method to extract an approximation

of the three-body potential. In addition to its immediate uses as an approximation of the potential, this can be used in conjunction with an *ab initio* potential to gain an even better understanding of the system.

In order to solve the problems presented in this document, a method of nonlinear fitting will be employed, fitting data calculated from guesses of functions to experimental data. Though the two problems presented - extracting velocity-depenent cross sections and three-body potentials - are somewhat different, the essential methodology remains the same. Entirely generally, regardless of the specific problem, some set of laboratory data, $g(y)$ will be required. In order to discover the desired function, some $f(x)$, we will develop a relation,

$$g(y) = h(f(x), y). \tag{4}$$

. Equation 12 in chapter 3 gives a specific example of this sort of relation, allowing us to easily calculate the line shape ratio from the velocity-depedent cross section, although reversing this calculation is difficult.

In both of the problems presented here, this equation cannot easily be inverted to discover $f(x)$ in terms of h and g (and if this inversion were possible, this method would not be required).

We will write $f(x)$ in a form such that it depends on some variable parameters $a_1, ..., a_n$. Beginning with an initial guess for these parameters, we can calculate a $g(y)$ to compare to the lab data. Specifically, in chapter 3, we will calculate the line shape ratio as a function of the detuning, given a velocity-dependent cross section while in chapter 4, we will calculate the rate constant as a function of the final vibrational and rotational state, given a three-body potential function. In each of these cases, we will then use the Levenberg-Marqardt algorithm [8,9] - a least squares fitting algorithm - to iteratively approach a best fit solution by finding a minimum in χ^2.

CHAPTER 3

Velocity-Dependent Cross Sections

1. Introduction to the Problem

In this chapter, we will present our method for extracting velocity-dependent cross sections from spectral line data. In order to do this, we need to relate the velocity-depedent cross section to the experimental data we can collect. We could take a simple average over equation 3, but we can get a much better fit, by fitting a series of data rather than a single point. This means that we will need to discover the probability of a particular collisional velocity given an experimentally adjustable parameter, the laser detuning from resonance. The laser detuning is the difference in frequency between the laser frequency and that of a laser tuned so that the maximum number of particles are excited. By finding this probability, of a particular collision velocity given the detuning, we can integrate over equation 3 and relate the integral over the collision velocity of the velocity-dependent cross section to the velocity averaged rate constant as a function of laser detuning.

To find this probability, we will need to fully develop the theory behind the Velocity Selection by Doppler Shift (VSDS) technique, which involves exciting molecules with a selected velocity component along the direction of the laser. [10-12] This chapter will make use of that theory to apply the fitting techniques mentioned in the previous section to this particular problem.

Once we have developed this theory, we will test this fitting method by fitting line shape ratios calculated from synthetic cross sections. That is, assuming a velocity-dependent cross section form, we will calculate a line shape ratio and then attempt to recover the original cross section. This allows us to know what the cross section should look like with a good fit, and further allows us to compare the quality of our fits to those of previous studies. [11,13] Unfortunately, these studies are in the Na_2-Xe system. However, for the purposes of the synthetic data, the only difference between these systems are the two system parameters. Fortunately, these parameters – r, the mass ratio of the target over the molecule and Γ, the homogenous linewidth – are simply numerical constants and do not affect the fitting process, so long as we are working with strictly synthetic data. As such, all artificial cross sections fit in this chapter will use the Na_2-Xe system.

Using our lab setup, the laser excites the lithium (or sodium) molecules. However, it does not excite all of those that pass through the beam of the laser. A molecule traveling at velocity v_L relative to the beam of the laser will view a first-order Doppler Shifted frequency

$$\nu' = \nu(1 \pm v/c). \tag{5}$$

Here the sign depends on the direction the molecule is traveling with respect to the laser (it is negative for particles moving away from the laser). If we call ν_0 the excitation frequency of a particle at rest with respect to the laser, then we can write the following:

$$v_L = (\frac{\nu - \nu_0}{\nu})c. \tag{6}$$

However, since ν_0 and ν are similar, we can rewrite this as

$$v_L = (\frac{\nu - \nu_0}{\nu_0})c, \tag{7}$$

introducing an error on the order of only 10^{-5}.[10]

This means that the detuning of the laser from resonance, $\nu - \nu_0$ determines the dimer velocity in the direction of the laser, v_{pz}.

Assuming that the unselected velocities follow the Maxwell speed distribution, we can express the probability of a given relative velocity v_r between the molecule and the collision partner as a function of the laser-selected velocity in the z direction. Here $P(A|B)$ indicates the probability of an event A occurring given an event B. The probability $P(v_r|v_{pz})$ is expressed below:

$$P(v_r|v_{pz})d^3v_t dv_{px}dv_{py} = (\frac{1}{2\pi r})^{\frac{3}{2}}(\frac{1}{2\pi})\exp(-\frac{v_{px}^2+v_{py}^2}{2})\exp(-\frac{v_t^2}{2r})d^3v_t dv_{px}dv_{py}. \tag{8}$$

Here, the p subscript refers to the primary molecule - the lithium (or sodium) dimer. The x, y, z subscripts refer to component of the velocity in the x, y or z direction. The t subscript refers to the target atom – the collision partner. All velocities are expressed in dimensionless units $s_p = \sqrt{\frac{kT}{m_p}}$. m_p refers to the mass of the molecule, and $r = \frac{m_p}{m_t}$ the mass ratio. In this chapter we will use $r = .3205 = \frac{m_{Na_2}}{m_{Xe}}$.

Unfortunately, $P(v_{pz}|v_L)$, the probability of exciting a molecule with velocity component v_{pz} given a detuning v_L, is not a delta function. That is, a given detuning does not select out only a single value of v_{pz}, and we therefore have to include $P(v_{pz}|v_L)$ in our calculations. The natural lineshape is a Lorentzian, and the Maxwell speed distribution is a Gaussian, so the probability is a product of these:

$$P(v_{pz}|v_L) = \exp(-v_{pz}^2/2)\frac{\Gamma/\pi}{\Gamma^2+(v_L-v_{pz})^2}V^{-1}(v_L,\Gamma), \tag{9}$$

where

$$V(v_L,\Gamma) = \int_{-\infty}^{\infty} dv_{pz}\exp(-v_{pz}^2/2)\frac{\Gamma/\pi}{\Gamma^2+(v_L-v_{pz})^2}. \tag{10}$$

Here $V(v_L,\Gamma)$ is the Voigt profile; it is used to normalize the distribution where Γ is the homogeneous linewidth and in this chapter we will use $\Gamma = .03\text{cm}^{-1}$,

the value for the Na_2-Xe system. [11] By combining these two, we can express $P(v_r|v_L)$, the probability of a collision velocity given a laser detuning, as

$$P(v_r|v_L) = \int_{-\infty}^{\infty} dv_{pz} P(v_r|v_{pz}) P(v_{pz}|v_L), \tag{11}$$

the probability of a collision velocity given a laser detuning, the relationship we stated a need for at the beginning of the chapter. This will allow us to establish a relationship between the velocity-dependent cross section and the line shape ratio.

Finally, we can express the experimentally obtainable line shape ratios in terms of known quantities and the velocity-dependent cross section $\sigma(v_r)$. Recall that $k(v_r) = v_r\sigma(v_r)$. From equations 3 and 11, we can take the average in relative velocity giving us the following:

$$\overline{k}(v_L) = \langle v_r\sigma(v_r)\rangle = \int dv_r P(v_r|v_L) v_r\sigma(v_r) \tag{12}$$

where χ^2 is calculated on $\overline{k}(v_L)$. Note that as shown in equation 2, $\overline{k}(v_L)$ is proportional to the ratio of the populations of a given final state and the initial excited state. This is in turn proportional to the satellite to parent line shape ratio of that level and we will treat $\overline{k}(v_L)$ and the line shape ratio interchangeably in this document.

We can assume a functional form for the cross section and calculate a value for $\overline{k}(v_L)$ to compare with the experimental values. Then, using least squares fitting, we can attempt to extract a velocity-dependent cross section. For much of this chapter, we will test this method by fitting synthetic data – that is, we will invent a form for a cross section as a function of collision velocities ranging between 0 and 4 s_p (the values used in references [11,13]), such as the first set of data in figure 3. From this we will calculate a line shape ratio as a function of detuning varying between 0 and 4 s_p, such as the first set of data in figure 4. We will

treat this as our experimental data. Then we will calculate cross sections from a functional form (see equation 13 below), which might look like the cross sections in figure 6. From these we will calculate line shape ratios such as those in figure 5. By comparing these line shape ratios to the synthetic one from figure 4, we can iteratively improve our fit to the line shape ratio and as a consequence, to the cross section, as figures 5 and 6 show. Lastly, the fit converges to a final fit, such as figures 3 and 4 show.

In order to determine that a fit has converged, we measure the improvement in χ^2 from one iteration to the next. When it has failed to improve by more than .1% for 20 consecutive iterations, we end our fit. While 20 is sometimes unnecessary, our fits go quickly enough that this is feasible.

Further note that although in our fitting process we fit data ranging from 0 to 4 s_p, in qualitatively examining the success of our fits, we pay most attention to the region between .7 and 3.5 s_p. This is because outside these limits, the quality of the data begins to degrade rapidly. [11,14]

More simply, the fitting process is a cycle of calculating $\overline{k}(v_L)$ from $\sigma(v_r)$, comparing the calculated $\overline{k}(v_L)$ with the experimental (or synthetic) data and using this comparison to adjust $\sigma(v_r)$.

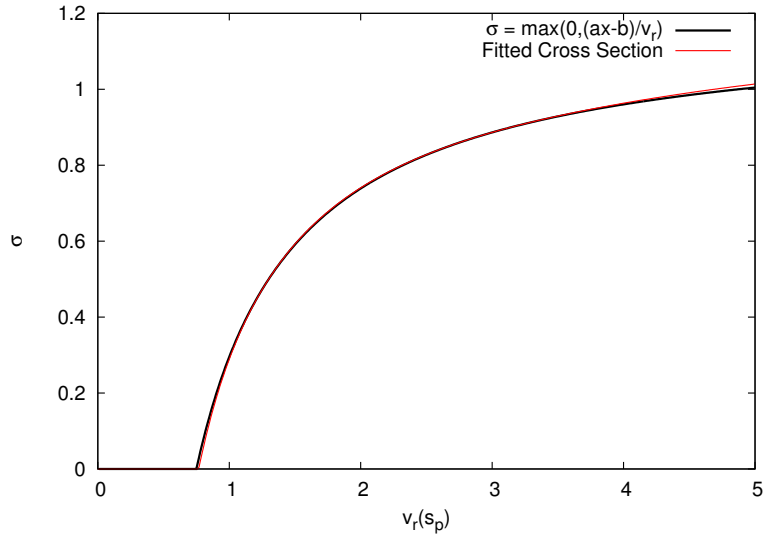

Figure 3: The cross section corresponding to a fit to a synthetic line shape ratio generated from a linear rate constant.

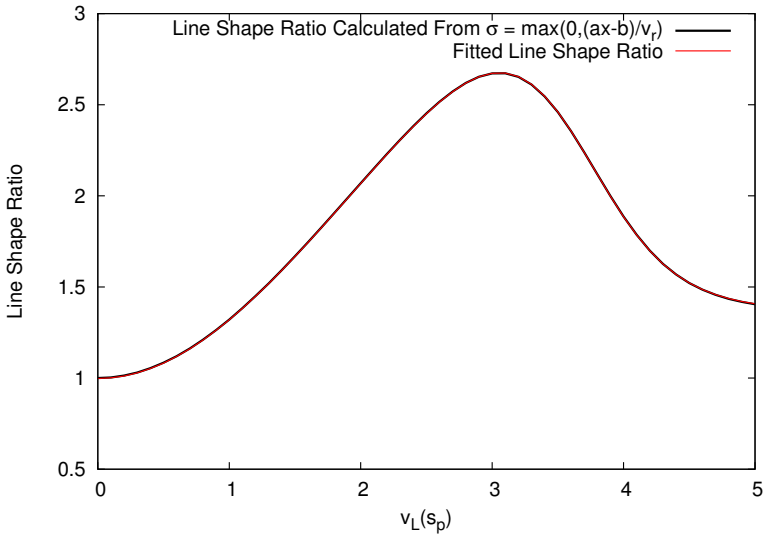

Figure 4: The synthetic line shape ratio and the fit to it from figure 3.

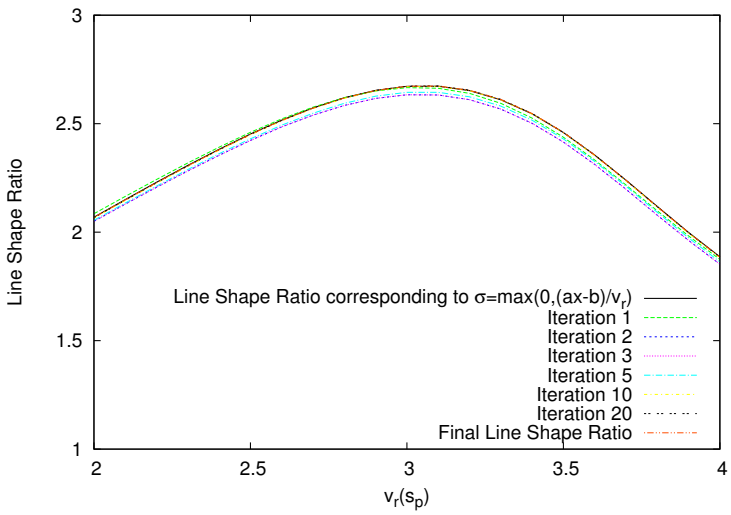

Figure 5: The fitting algorithm allows our calculated line shape ratios to iteratively approach lab data. Each iteration has a χ^2 less than or equal to the one before it. Note that this image shows a smaller portion of the line shape ratio than does figure 4

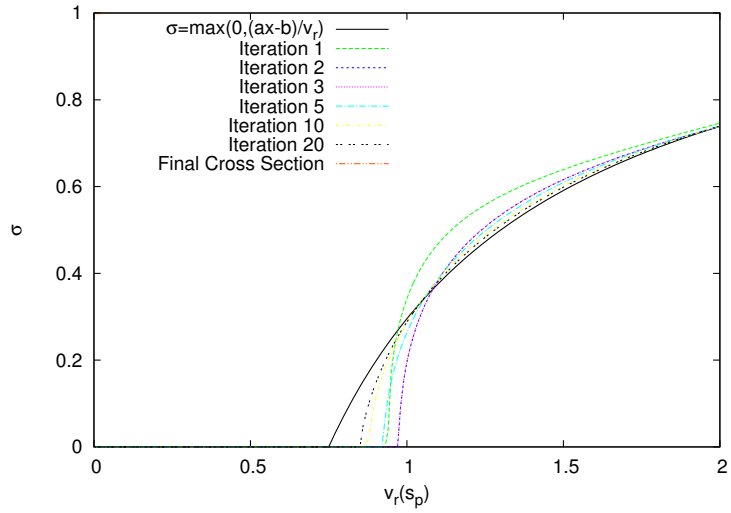

Figure 6: As is the goal of this fitting process, the fit to the cross section iteratively approach the actual cross section. Note that this image shows a smaller portion of the cross section than does figure 3

Typically, we expect cross sections for rotationally and vibrationally inelastic collisions - the ones this document is working with - to be zero up until an energy (or equivalently, velocity) threshold. Above that velocity, the cross section increases, peaks, and then falls [15]. To accommodate this, the functional form we choose is a polynomial times a power function times a negative exponential, all shifted by an adjustable cutoff velocity. The polynomial accounts for the rise before the exponential takes over and the function begins to decrease with increased v_r. More specifically, we use the form

$$\sigma(v_r) = e^{-\beta(v_r - v_0)^\gamma} \sum_n s_n (v_r - v_0)^{n+\alpha}. \tag{13}$$

In this chapter, all references to polynomials refer to the polynomial in this functional form. That is to say, a functional form with a first degree polynomial looks like

$$\sigma(v_r) = \left[(s_0 + s_1(v_r - v_0))(v_r - v_0)^\alpha\right] e^{-\beta(v_r - v_0)^\gamma}. \tag{14}$$

Further, except where stated otherwise, we will use a functional form with a second degree polynomial.

2. Initial Results

In order to test the method, we first attempted to fit artificial data. To do this, we assumed a form for the velocity-dependent cross section, $\sigma(v_r)$. To simulate lab data, we began with a cross section form and calculated the line shape ratio using equation 12. Inserting this line shape ratio into the fitting program as synthetic lab data, we used our program to fit that line shape ratio and attempt to recover the original velocity-dependent cross sections. To test this process, we fit 18 different artificial cross sections. Three representative examples of these fits are shown below and in figures 3 and 4 above. We focus on these here because

most the work we did, extracting velocity-dependent cross sections from artificial line shape ratios, was done with these three.

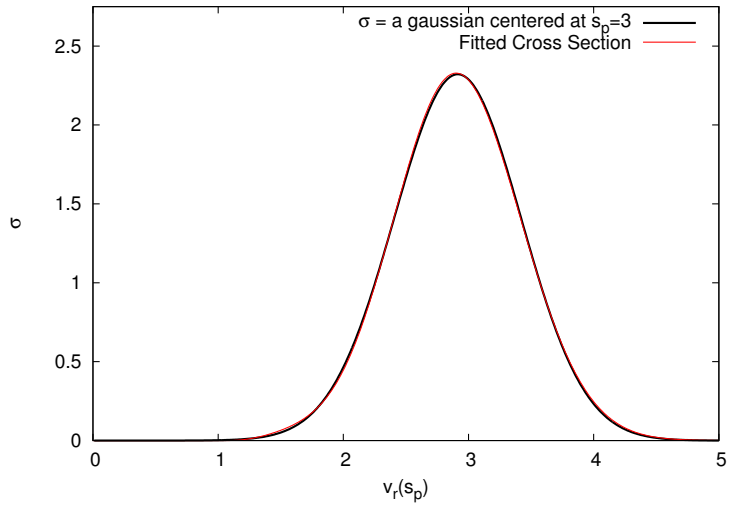

Figure 7: A fit to a synthetic line shape ratio generated from a cross section with the form of a gaussian.

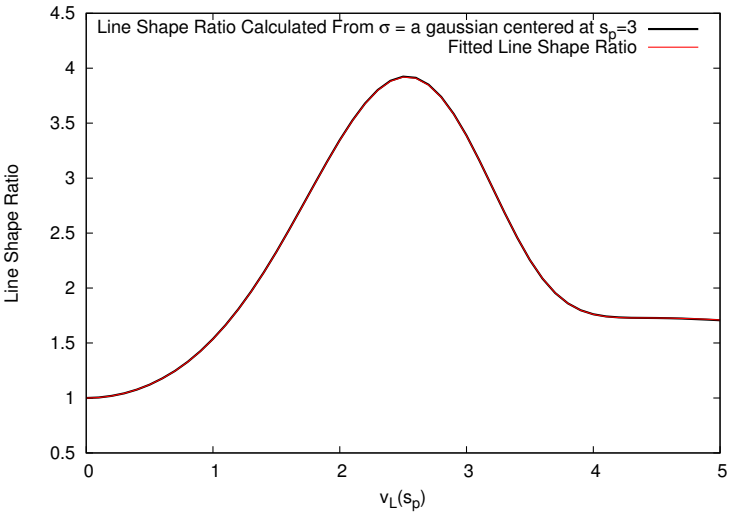

Figure 8: The synthetic line shape ratio and the fit to it from figure 7.

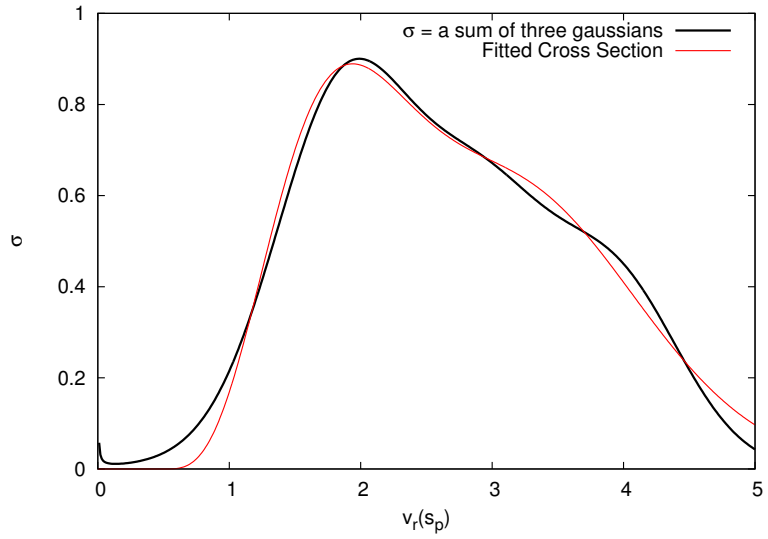

Figure 9: A fit to a synthetic line shape ratio generated from a cross section equal to a sum of three gaussians.

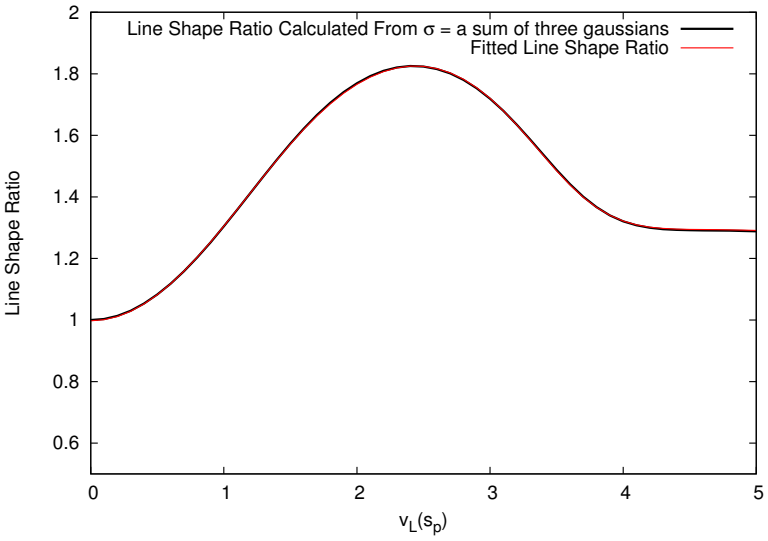

Figure 10: The synthetic line shape ratio and the fit to it from figure 9.

In figures 3 and 7, the fits are nearly perfect - in figure 3, the root mean squared difference between the original cross section and our fit to it was 0.00874, while in figure 7 it was 0.00938. A good fit here is not unexpected, because the functional form of this artificial cross section was mathematically reasonably simple and equation 13 could model these forms exactly. However, that the fit was nearly perfect is encouraging. Our function didn't fit the sum of gaussians in figure 9 as well - the root mean squared difference was 0.19616. While the fit approximated the function and was in fact a good fit, some of the detail in the curve was not captured by the fit.

These three images are indicative of the quality of the rest of the fits to artificial data: the fits were good across the board, with some nearly perfect and others less successful at fitting the details of the artificial cross section.

3. Varying Initial Values of the Parameters

As we showed in chapter 2, the fitting routines require initial values for each of the parameters in the functional form. If these original guesses are too far from the best fit, the fitting routine might get stuck in a local χ^2 minimum and not find the global minimum. However, even assuming that the initial values are reasonable, χ^2 space can be complex enough that two fits with similar initial values for the parameters proceed to different χ^2 minima. Table 1 and figure 11 show ten different fits to our artificial experimental data, using Monte Carlo methods to select initial conditions within 300% of one another. The cross section that we used in this test was a sum of three gaussians, which we chose because it provided a clear example of the phenomena that we will show in this section.

test	χ^2	rms diff
1	0.182532	0.172781
2	2.694160	0.077255
3	2.342427	0.121407
4	1.862516	0.196166
5	0.215976	0.029782
6	0.197397	0.028413
7	0.193982	0.166480
8	13.320322	14.950305
9	1.735010	0.074806
10	0.214705	0.028726

Table 1: The χ^2 and root-mean-square (rms) differences from the actual cross section for 10 tests with different initial values for the parameters. Although 5 tests have low χ^2 values, only 3 have low rms differences from the actual data

What we see here is that although five of these tests have comparably good χ^2 values, three of them have far lower rms differences than the other two. That five of these have a higher χ^2 value is not concerning, since we will know the χ^2 value of fits of experimental data and can use this as a figure of merit, to exclude these runs as poor fits. We examine the remaining five fits in figure 11.

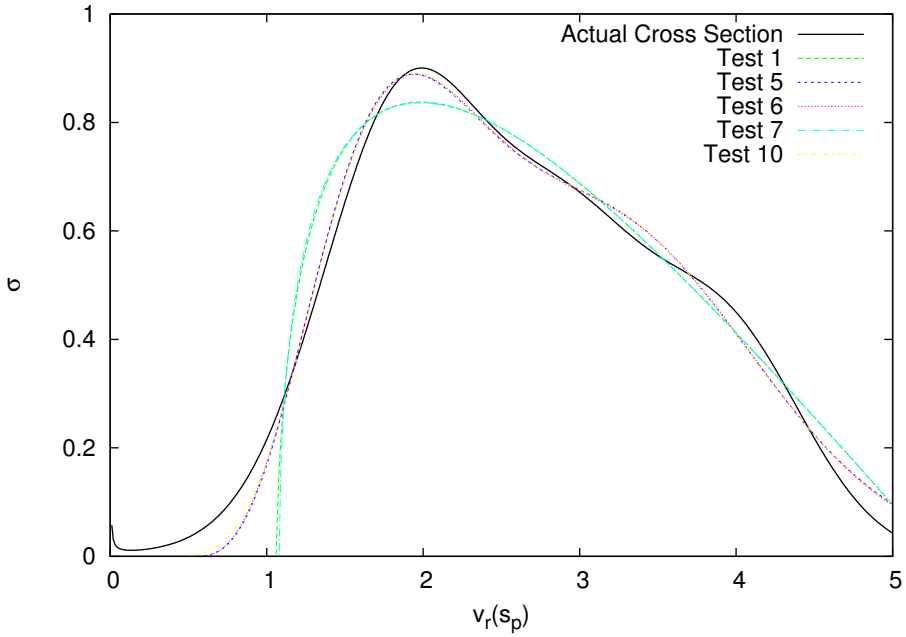

Figure 11: Tests 5,6 and 10 Fit this sum of three gaussians much more closely than tests 1 and 7, despite all having approximately equal χ^2 values

What figure 11 shows is that although 5 of the tests had approximately equal χ^2 values, only 3 of them were good fits. What this means is that two χ^2 minima produced similarly good fits to the artificial line shape ratio, while representing qualitatively different velocity-dependent cross sections. In other words, the solution to this problem is non-unique. There are of course almost always many local minima, but most can be ignored because they have much higher χ^2 values than the minimum around the actual cross section. These minima though have comparable χ^2 values and thus without *a priori* knowledge of the actual cross section, we have not yet found a way to distinguish between these minima. This is obviously a significant problem, since fits to experimental data could result in multiple cross sections with no obvious way to select the best fit to the corresponding physical cross section.

4. Non-Unique Solutions

We use two methods to select the best solution when there are multiple fits with comparably good χ^2 values and qualitatively different shapes. The best solution is the cross section that has the lowest rms difference from the actual cross section. Of course, when fitting experimental data, this comparison is not possible.

For the functional form of the cross section used here, we typically use a second degree polynomial. However, by varying the degree of this polynomial we can radically change χ^2 space, in fact changing its dimensionality, since each coefficient in the polynomial is a different parameter and corresponds to an additional dimension in χ^2 space. By making multiple fits with multiple different polynomial degrees, we can sometimes find which of our multiple solutions is best by finding the one that is common to all the cross sections with polynomials of differing degrees.

There will always be a χ^2 minimum around the shape of the actual physical cross section. The fit approaches that minimum, the closeness to which is measured by χ^2. If we change χ^2 space by changing the degree of the polynomial in the functional form we are using, there should always be a minimum somewhere near the actual cross section, although we can only approach this minimum as closely as our functional form will allow. These alternate minima may not exist or be nearly as good when we change the degree of the polynomial, however. So the solution that is common to fits from each polynomial degree is likely to be the correct one, assuming there are not multiple that fit this criterion – that is, assuming that there are not several qualitatively different fits that are common to each of the polynomial degrees.

We will demonstrate this method with fits to the lineshape ratio calculated from the cross section that is the sum of three gaussians. There were 10 fits for each polynomial degree between 0 and 5, inclusive.

Test	0th	1st	2nd	3rd	4th	5th
1	0.615395	2.663361	0.183895	2.751262	0.280156	**0.086788**
2	11.254291	2.274268	0.178675	0.382710	0.297256	0.469061
3	437.791292	2.294486	**0.152692**	21.717153	0.202173	0.460620
4	11.254548	2.285769	0.178218	0.322171	**0.066442**	0.296402
5	3.005293	2.278412	0.454139	1.231025	**0.064400**	0.110287
6	2.914170	2.006532	0.216095	**0.064359**	**0.062129**	**0.091152**
7	562.375994	2.285275	0.221697	0.241758	47.922664	**0.088038**
8	2.684091	2.858189	**0.147063**	7.379343	126.586939	0.926681
9	11.250289	1.082303	**0.153040**	0.994106	0.290001	0.276563
10	468.813735	3.074538	**0.083039**	**0.066345**	7.137325	0.276248

Table 2: χ^2 values for 10 different fits for cross sections with 0th- through 5th-degree polynomials. Each column has a different degree of polynomial in the fit, varying from a 0th degree polynomial in the 2nd column from the left, to a 5th degree polynomial in the column on the far right. The fits in bold are shown in figures 12-15. They were selected on the basis of χ^2 value.

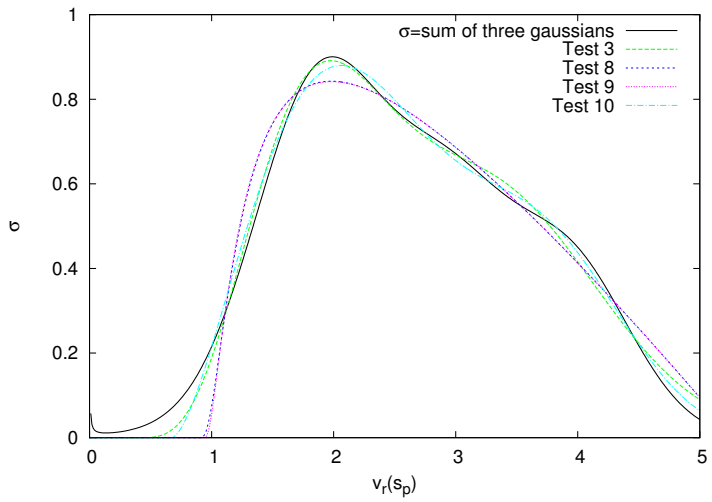

Figure 12: Fits with varying initial values for the parameters for a 2nd degree polynomial in the cross sections. These fits correspond to the bold χ^2 values in table 2.

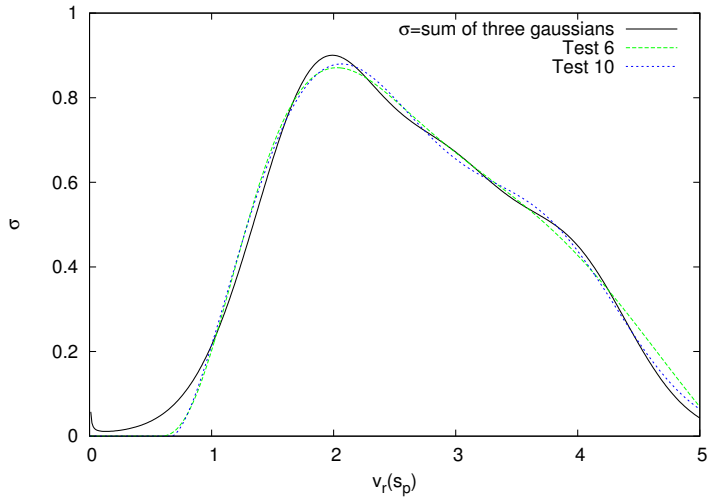

Figure 13: Fits with varying initial values for the parameters for a 3rd degree polynomial in the cross section. These fits correspond to the bold χ^2 values in table 2.

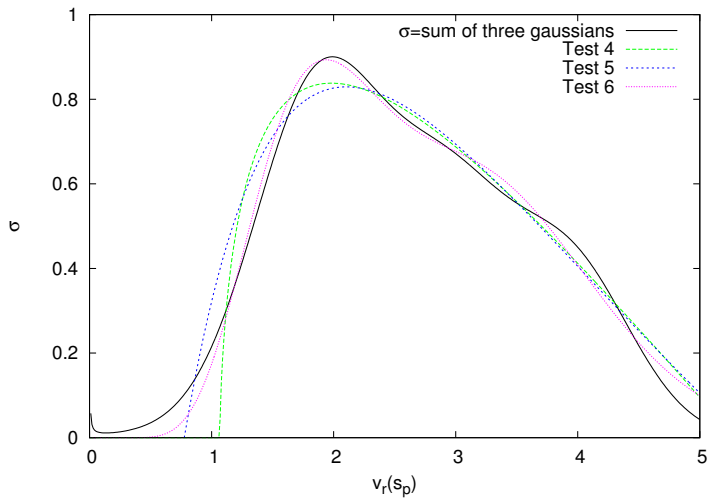

Figure 14: Fits with varying initial values for the parameters for a 4th degree polynomial in the cross section. These fits correspond to the bold χ^2 values in table 2.

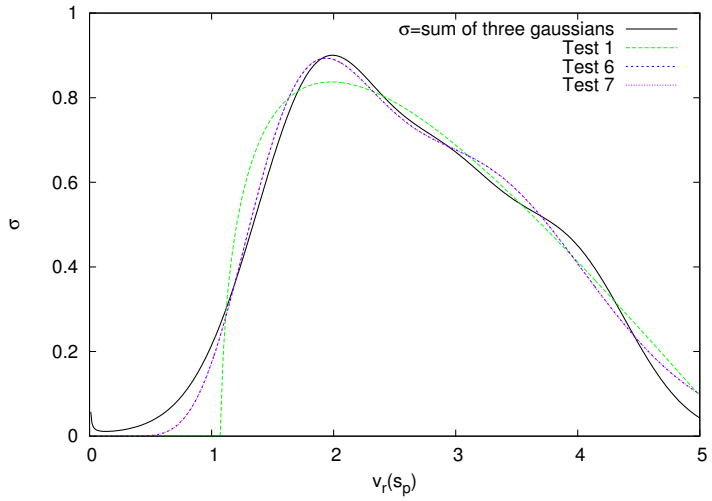

Figure 15: Fits with varying initial values for the parameters for a 5th degree polynomial in the cross section. These fits correspond to the bold χ^2 values in table 2.

For the cross section with the third degree polynomial, the alternate minimum – the one that has a comparably low χ^2 value and a qualitatively different shape from the actual cross section – does not show up at all. On running more tests, we found that this the fits with the third degree polynomial never converged to this alternate minimum. However, the 4th and 5th degree polynomial fits do. Shown in figure 16 is 10 more fits with a third degree polynomial, where we see that again, the alternate minimum did not appear.

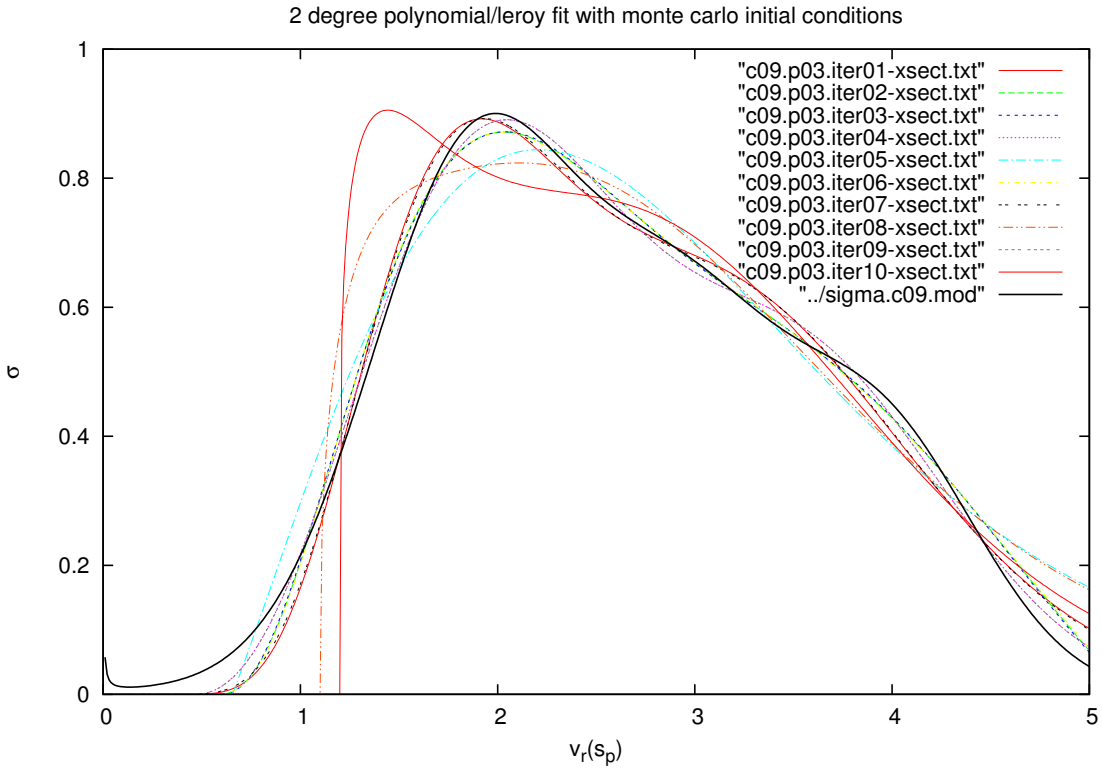

Figure 16: 10 more fits with a 3rd degree polynomial in a cross section. Here, although test 8 appears to be similar to the false minimum, its χ^2 value is 10 times that achieved by other fits in the set so it would be thrown out were it to show up in a fit to experimental data

This method of varying the polynomial degree in the cross section can be a good way of choosing the cross section that is shaped like the actual cross section, but sometimes it might be insufficient. Fortunately, there is another method at our disposal.

The other method we can use to select the best solution is by comparing to another solution to this problem that was simultaneously developed in our group. Graduate Student Paula Matei uses a full Fourier deconvolution method to extract velocity-dependent cross sections from experimental (or synthetic) line shape ratios. While her method completely avoids the risks of non-unique solutions, as a polynomial it is not always able to fit the data as well as the method shown in this document. [14]

5. Polynomial Degree

Our functional form for the cross section has a polynomial multiplied by an exponential. By varying the degree of this polynomial, we can try to eliminate false χ^2 minima from the previous section, but as the polynomial degree increases, the number of false minima increases. We have found a 5th degree polynomial is the maximum useful degree. Increasing the number of parameters can allow us to fit more complex functions, and given the complex nature of physical data, increasing the number of parameters can be helpful in that it gives the function more flexibility. The tradeoff is that as the number of parameters increases, so does the complexity of χ^2 space. Unfortunately, as the dimensionality increases, so does the number of χ^2 minima and the number of alternate solutions. If we increase this too far, there are so many minima that the function stops converging to the actual cross section.

In order to demonstrate this, we made many fits of several artificial line shape ratios corresponding to a constant cross section and the cross section in figures 5,7 and 9, varying polynomial degree between 0 and 15.

We used the rms difference between the actual cross section and the results of our various fits as a figure of merit to indicate how good each fit was at capturing the constant cross section. We measured χ^2/ν where ν is the degrees of freedom of the fit,equal to the number of data points minus the number of parameters. We used this, since this is the only figure of merit we would have access to when fitting experimental data.

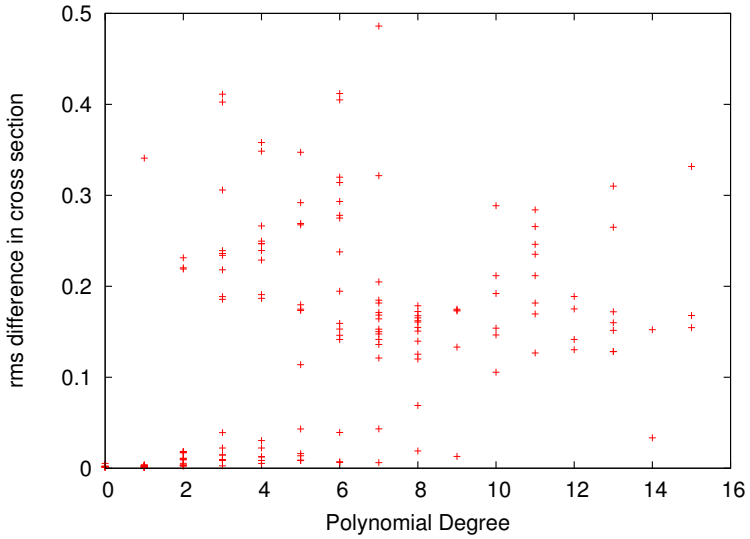

Figure 17: rms difference between cross sections from fits and a constant cross section.

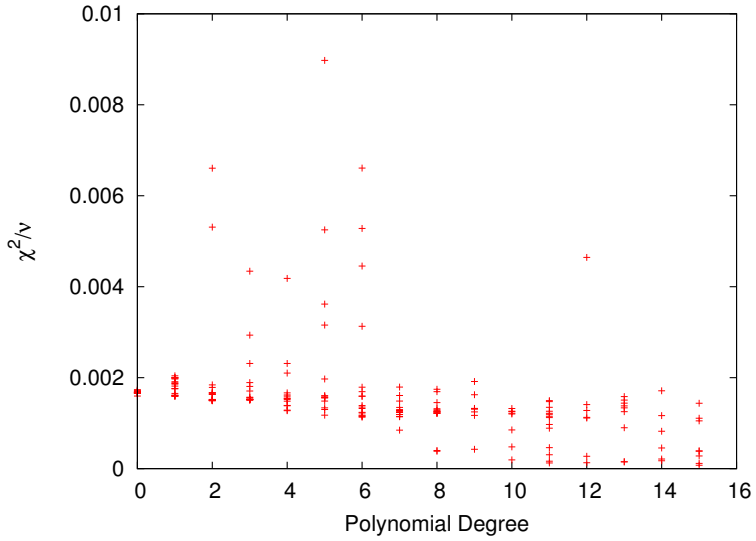

Figure 18: χ^2/ν for fits to a line shape ratio calculated from a constant cross section.

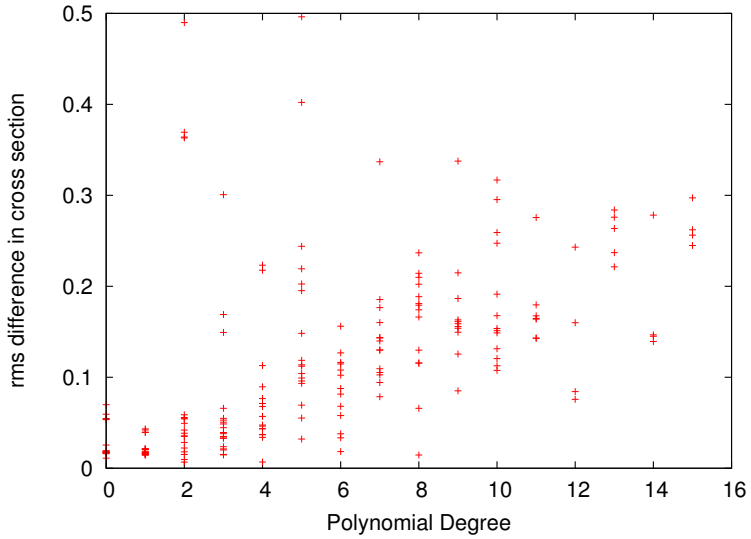

Figure 19: rms difference between cross sections from fits and a cross section calculated from a linear line shape ratio.

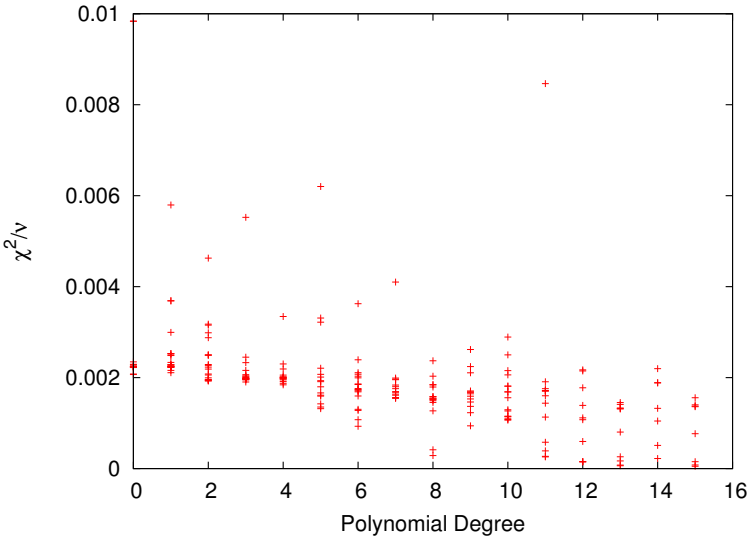

Figure 20: χ^2/ν for fits to a line shape ratio calculated from a linear line shape ratio.

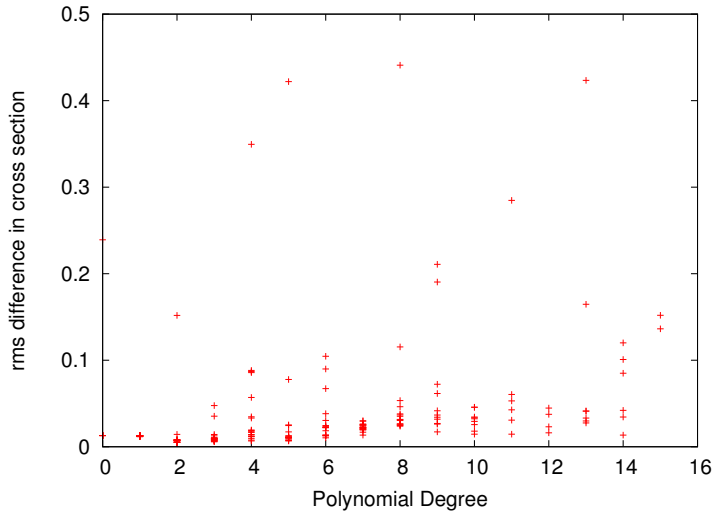

Figure 21: rms difference between cross sections from fits and a cross section that is a gaussian centered at $s_p = 3$.

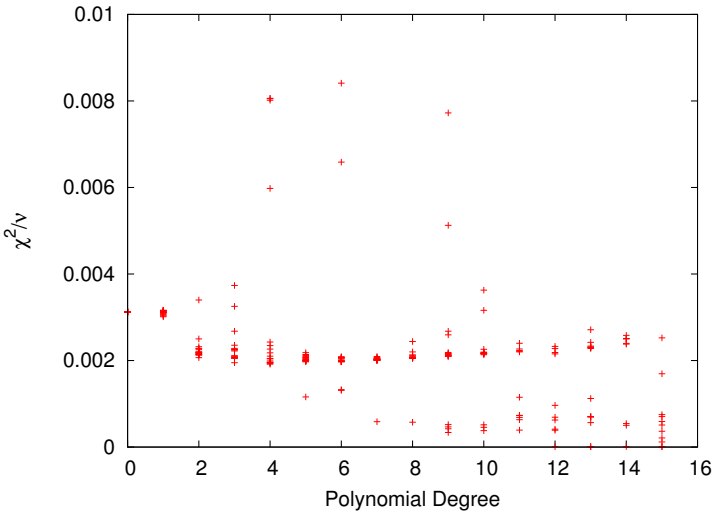

Figure 22: χ^2/ν for fits to a line shape ratio calculated from a cross section that is a gaussian centered at $s_p = 3$.

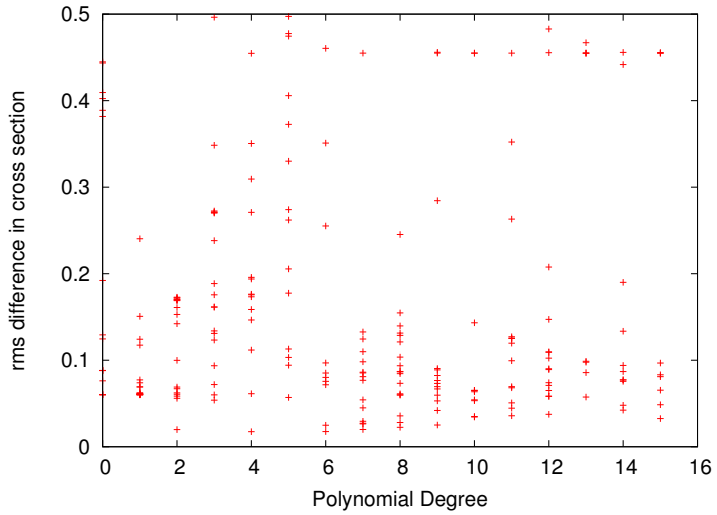

Figure 23: rms difference between cross sections from fits and a cross section that is the sum of three gaussians.

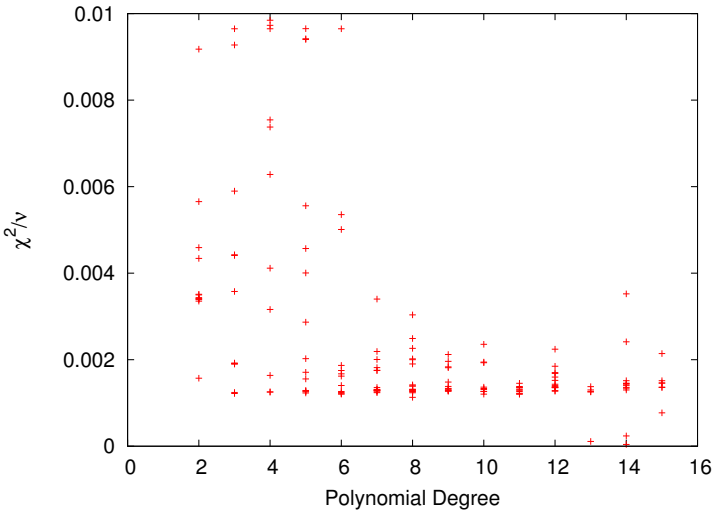

Figure 24: χ^2/ν for fits to a line shape ratio calculated from a cross section that is the sum of three gaussians.

What these graphs show is that after excluding the bad fits, of which there are always some, increasing the polynomial degree initially allows the fit to improve. However, at some point the quality of the actual fit degrades, though χ^2/ν may not reflect this. That is to say, the function is finding false minima with low χ^2/ν but high rms difference.To resolve this, we can use comparison with fits with varying polynomial degrees and comparison with the Fourier deconvolution method. Further, it doesn't make sense to increase the polynomial degree too far when fitting experimental data. Above a 5th or 6th degree polynomial, we run the risk of having a fit with very low χ^2/ν that does not reflect the actual cross section very closely. This is because, as we can see most clearly in figures 17-20, although the quality of the fit as measured in rms difference can degrade after this degree, it is entirely possible to get extremely low χ^2/ν. This means that we run the risk of false minima confusing our fit to a degree that it may be hard to extract meaningful information.

6. Experimental Fitting

We made fits of experimental data with a cross section form with varying polynomial degrees. Figure 25 shows that the fits with the polynomial in the cross section with degree 2 and above approach the same fit, indicating the fit is unlikely to improve with higher degree polynomials in the cross section functional form. Also included in this image is the fit achieved by the Fourier deconvolution method discussed in section 4 of this chapter. As figure 25 shows, they agree very closely between 1.5 and 3.5 s_p and reasonably well between .7 and 1.5 s_p. As we discussed earlier in this chapter, outside of this range, the data is not particularly trustworthy and so we don't expect any particular agreement.

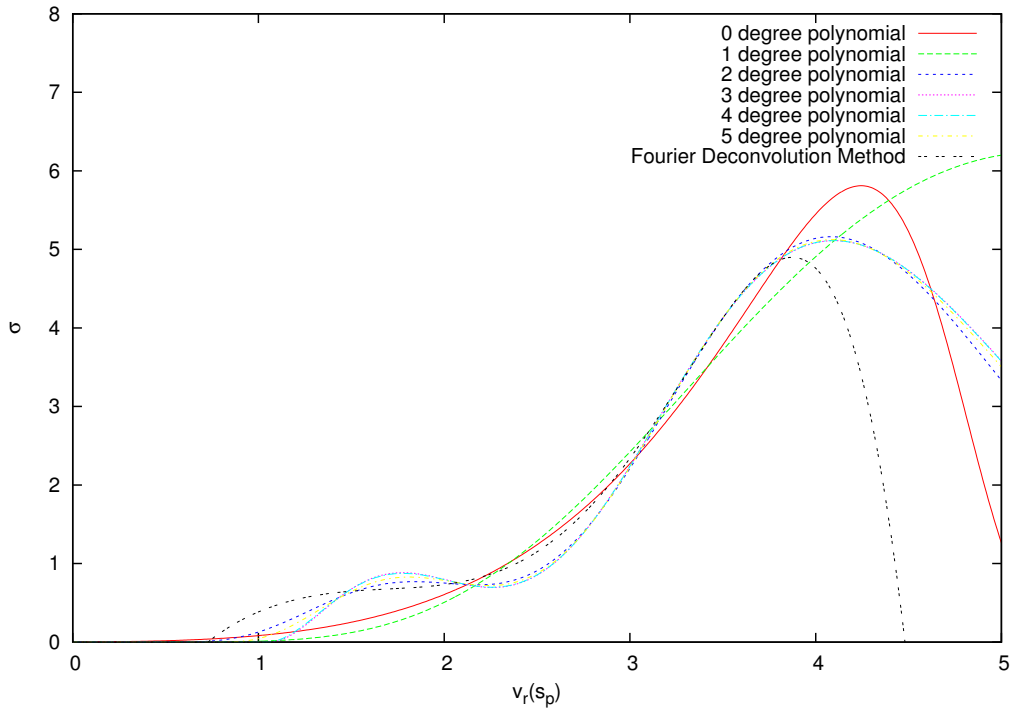

Figure 25: Extracted Cross Section for $v_i = 2, j_i = 11 \rightarrow v_f = 2, j_f = 15 (\Delta j = +4)$ data

By both varying the polynomial degree and comparing with the Fourier deconvolution method, we have verified our success at extracting a velocity-dependent cross section from experimental data.

CHAPTER 4

Three-Body Potential Functions

The velocity-dependent cross section gives us an understanding of the effects of relative velocity on a collision. A three-body potential function, however, can give us a much better understanding of the collision dynamics. That is, while a potential function contains no dynamics explicitly, it provides the forces that give rise to the dynamics.

1. Introduction to the Problem

We use Quasi-Classical Trajectories (QCT) to create artificial rate constant results. In this method, initial energy levels in vibration and rotation are chosen to match allowed quantum values. We use Monte Carlo methods on many trajectories to average over initial conditions. We repeat this process for several selected collision energies. We then use the classical equations of motion to integrate over each trajectory and solve for the final rotational and vibrational state. Finally, we "bin" these energy states into the nearest quantum energy state. [16-18]. In order to do all of this, an implementation of the Levenberg-Marquardt algorithm written by Steve Coppage was used. [16]

This process allows us to calculate the cross sections for each final state at each velocity, since this is proportional to the number of trajectories that result in each state. Then, by making a discrete approximation of the integral in equation 12, we can calculate the thermally averaged rate constants, which we can compare to experimental values.

The molecular potential, $V(r, R, \cos\gamma)$ depends on r, the separation between the atoms in the molecule, R, the distance of the collision partner from the center of the molecule, and γ, the angle between the line connecting the center of the molecule and the collision partner (figure 26).

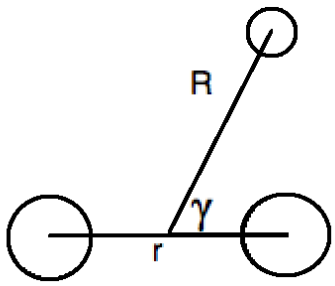

Figure 26: Coordinates used for collision calculations

2. Experimental and *Ab Initio* Data

Except where noted, fits in this chapter will use data from the Li_2-Ne system, measured after an initial excitation of the lithium to the $v_i = 0, j_i = 18$ level of the Li_2 ($A^1\Sigma_u^+$) state. [3] The equilibrium separation of the atoms in the molecule in this state is $r_0 = 3.108$. The data are shown in figure 27.

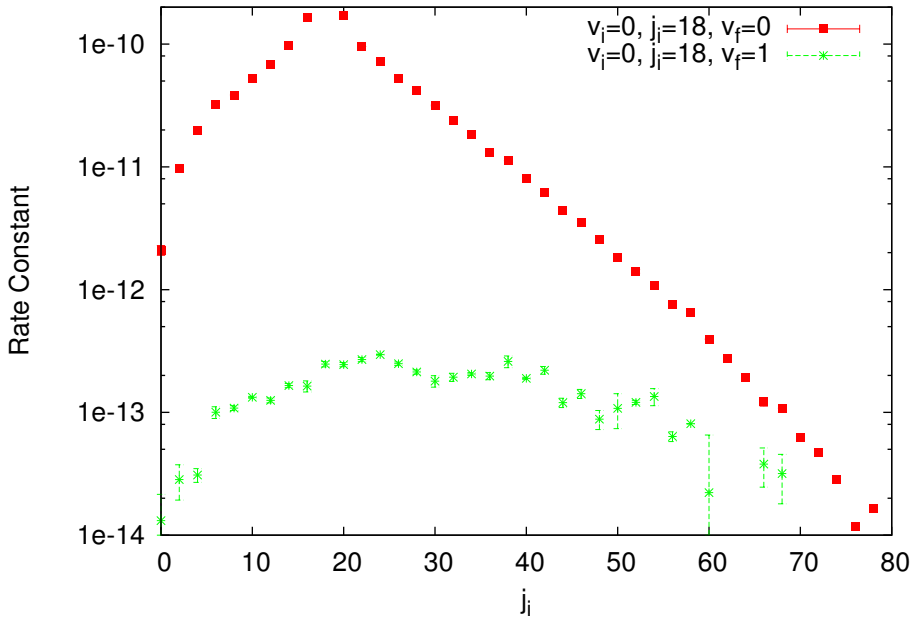

Figure 27: Experimental rate constants for $v_i = 0, j_i = 18$

The advantage of the Li_2-Ne system was twofold: there was an extensive amount of spectral data for this system produced in our lab, and we could make use of an *ab initio* potential surface for comparison with our fits.

The Alexander-Werner *abinitio* potential is an extremely useful tool, but it is not perfect. Particularly, comparison of calculations with experimental data implies that it is insufficiently anisotropic at long range and has an anisotropy that increases too quickly as R decreases. [3]

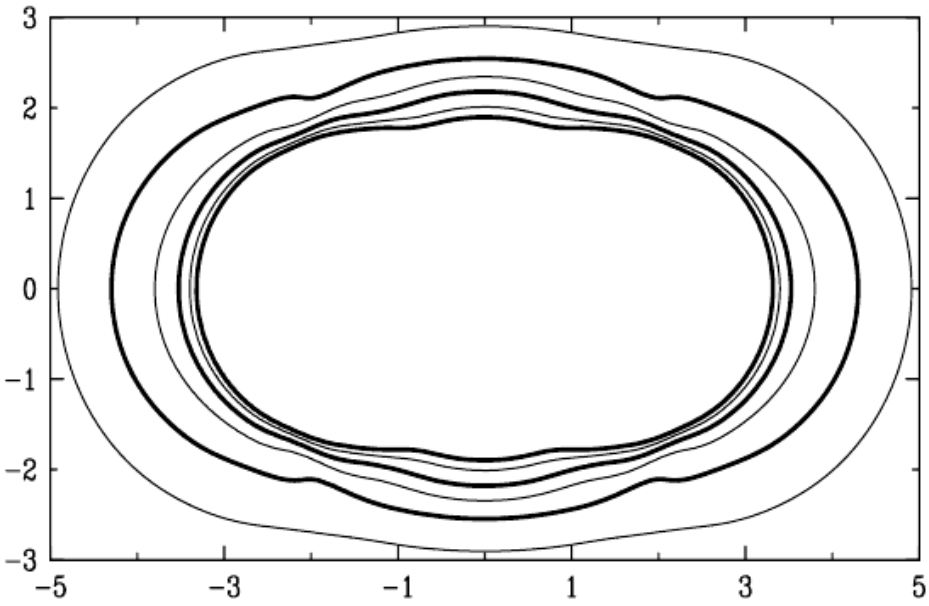

Figure 28: Contour plot of Alexander-Werner *ab initio* potential with fixed $r = r_0 =$ 3.108Å. There are contours every 500 cm^{-1}, with heavy contours at 1000, 2000, 3000 cm^{-1}. Image from Stewart *et al.*, 2010 [3]

3. Born Mayer Potential

To begin our tests, we used a very simple potential, the exponentially repulsive Born-Mayer potential added to a modified harmonic oscillator to provide for vibration in the molecule. [19,20]

$$V(r, R, \cos\gamma) = A(e^{-\alpha\sqrt{\frac{1}{4}r^2+R^2-rR\cos\gamma)}}+e^{-\alpha\sqrt{\frac{1}{4}r^2+R^2+rR\cos\gamma)}})+\frac{1}{2}m_{bc}(2\pi\omega(r-r_0))^2 \tag{15}$$

Here A and α are variable parameters, ω is the vibrational frequency in the $A^1\Sigma_u^+$ state, m_{bc} is the mass of the lithium molecule and r_0 is the equilibrium separation of the atoms in the molecule, and $r_0 = 3.108$Å

The advantage of this potential is that it is quite simple. We wanted to test both our mathematical methods and our computational routines. As a function intended for proof of concept, it was ideal. Further, if it provided even a slightly reasonable fit of the experimental data, we could try modifications of this potential to perhaps allow ourselves to better fit the data.

To keep the problem as simple as possible, we first attempted to fit rotationally inelastic data, ignoring all the vibrationally inelastic collisions.

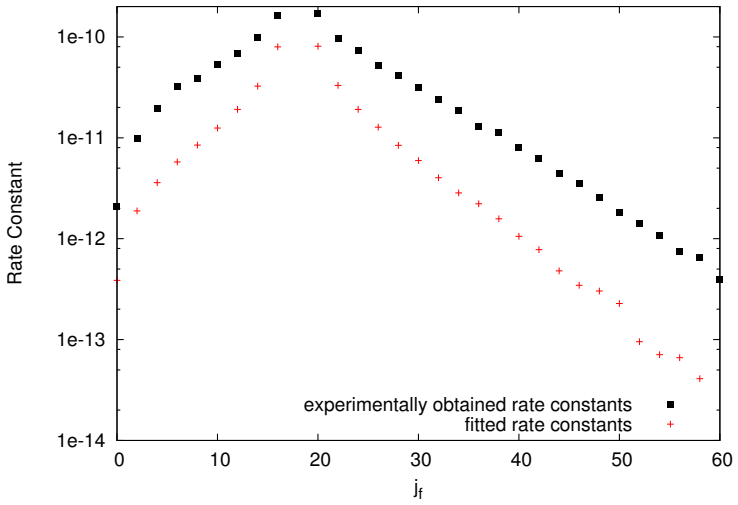

Figure 29: Fit of rotationally inelastic $v_i = 0, j_i = 18$ data with the born mayer potential. Note that the graph ends at $j_f = 60$, but the fit went through $j_f = 80$.

As a proof of concept, the Born-Mayer potential was adequate. The mathematical and computational methods worked well. However, as figure 30 shows, the fit to even just the rotationally inelastic data was very poor. Given how unsuccessful the fit to this data was, there was no need to add in more data, as attempting to fit to more data points can only worsen the fit to each one. Instead, we explored other potentials

One last thing to note was that as in the case of the velocity-dependent rate constant fitting, the final fit is dependent on the initial conditions, as a simply product of the complexity of χ^2 space. However, running many fits with varying input conditions resulted in very similar final fits for the Born-mayer potential, likely because this potential has only two parameters and so the 2-dimensional χ^2 space was much simpler.

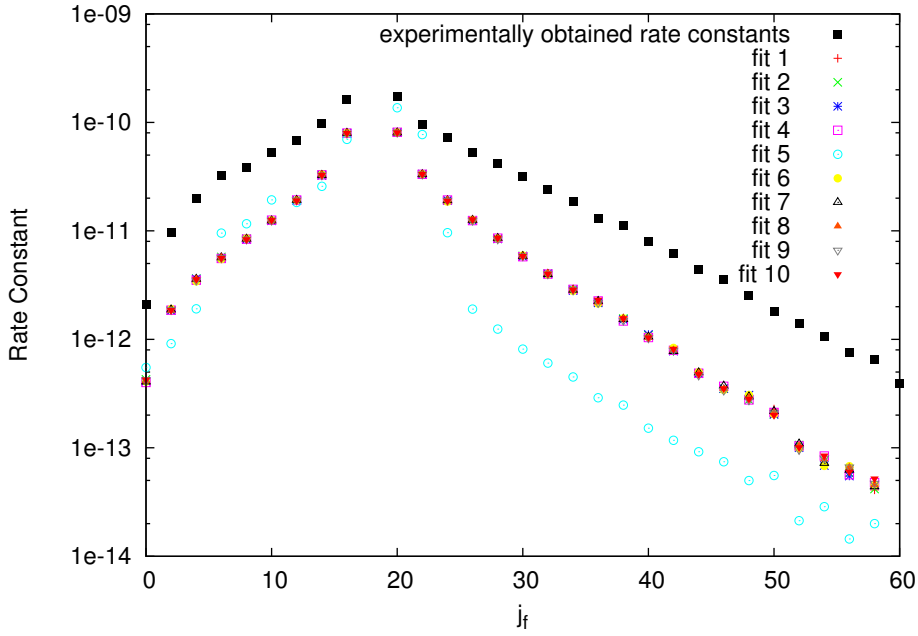

Figure 30: Several fits of rotationally inelastic $v_i = 0, j_i = 18$ data with the born mayer potential.

4. Spheroidal Potential

Another potential function we explored was a spheroidal form, such that

$$V = V_0 \exp(-\alpha R \sqrt{\cos^2(\gamma) + \beta \sin^2(\gamma)}). \tag{16}$$

This function has three parameters and so is a logical step up from the Born-Mayer potential. We decided to restrict this potential so that it does not accommodate vibration at all, to keep the function as simple as possible

As a functional form, the spheroidal potential was unsuccessful even at fitting simply rotationally inelastic data. As is clear from figure 31, the fits peak too high near $\Delta j = 0$ and fall off far too quickly at large Δj. This fit was in fact even worse than the Born-Mayer potential.

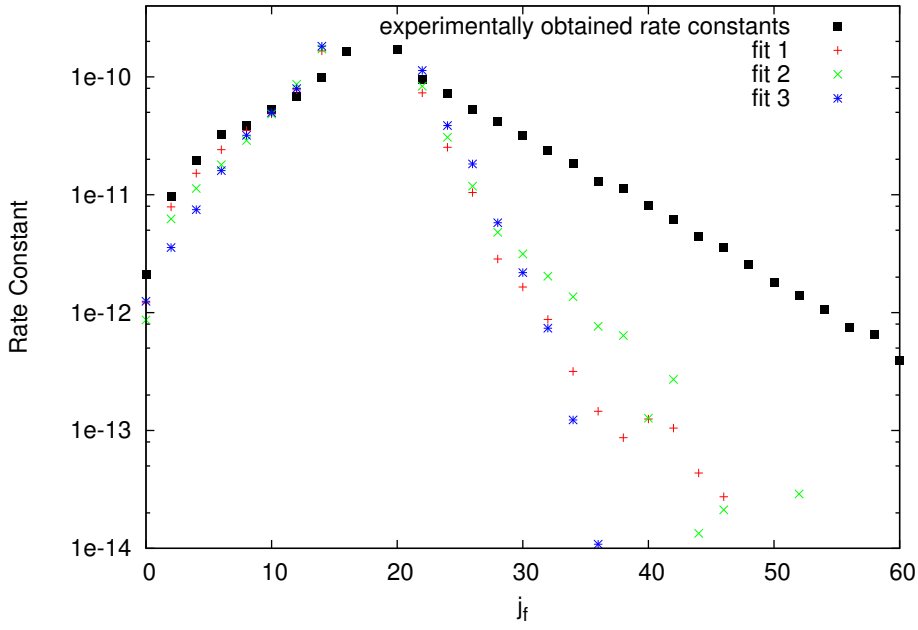

Figure 31: Three fits of rotationally inelastic $v_i = 0, j_i = 18$ rate constant data with the spheroidal potential.

5. Breathing Ellipsoid Potential

The next functional form we used was far more complex than the previous two, and increased the number of parameters to 6. We call this function a "breathing ellipsoid" - that is, an ellipsoid that changes in characteristic size as the molecule vibrates. [21] We call it this despite the fact that in actuality, the shape is allowed to be more complex than an ellipsoid. The explicit form is

$$V(r, R, \cos\gamma) = V_0 \exp\left[A\left(1 - \frac{R - \alpha(r - r_0)[1 + aP_2(\cos\gamma)]/(1 + a)}{L\{1 + aP_2(\cos\gamma)[1 + \beta(r/r_0 - 1)]\}}\right)\right] \quad (17)$$

The downside to this potential is that with six parameters and a much more complicated form, it was much more computationally expensive. In fact, these trajectories take on the order of 10 times longer to calculate, than Born-Mayer trajectories. However, these concerns are secondary to the fitting job it was able to do. We first attempted to fit the rotationally inelastic data.

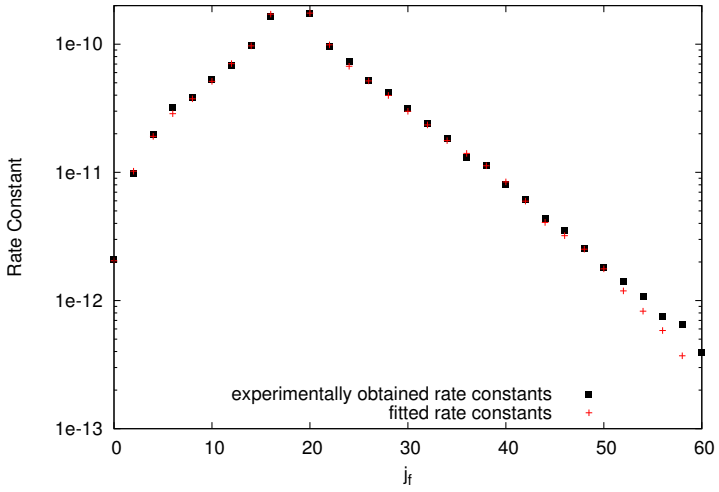

Figure 32: Fit of rotationally inelastic $v_i = 0, j_i = 18$ rate constant data with the breathing ellipsoid potential.

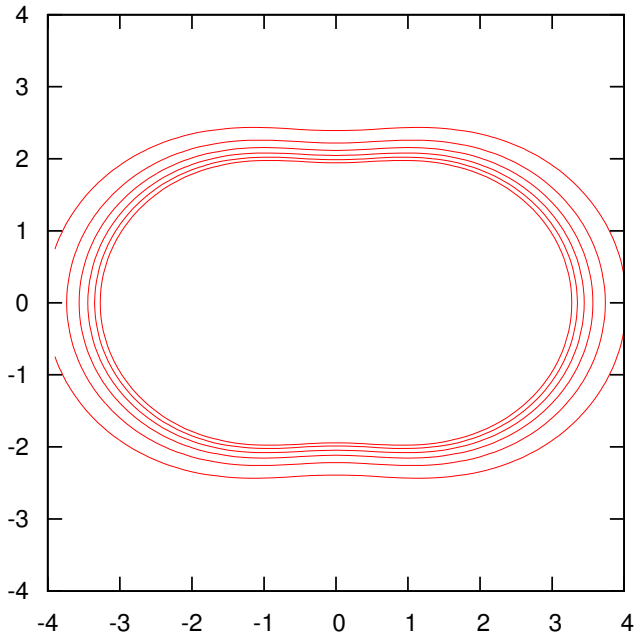

Figure 33: Contour surface for the potential corresponding to the fit in figure 32. The internuclear separation, r is fixed at $r = r_0$, and the contours are every 500 cm^{-1} from 500 to 3000 cm^{-1}.

With this fit, we have achieved our initial goal: we has successfully fit experimental rotationally inelastic rate constant data, and this fit is qualitatively quite good. Although the fit here is not perfect, it is much better than the previous two functional forms. It was good enough that it made sense to examine how successfully the potential could fit the vibrationally inelastic data.

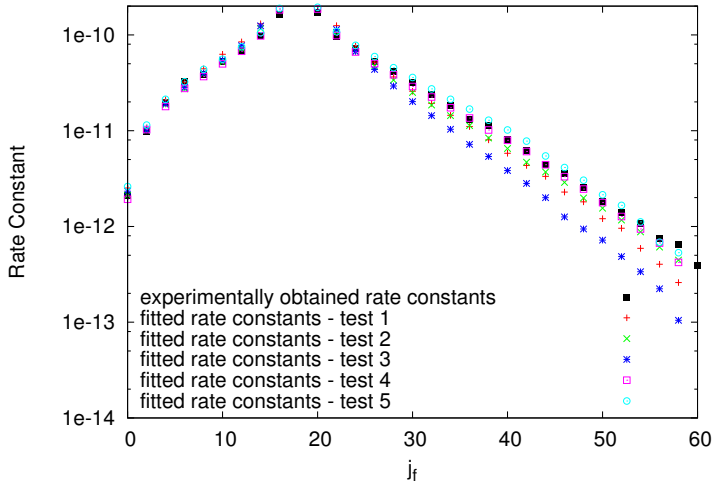

Figure 34: Fits of rovibrationally inelastic $v_i = 0, j_i = 18$ rate constant data with the breathing ellipsoid potential for $v_f = 0$.

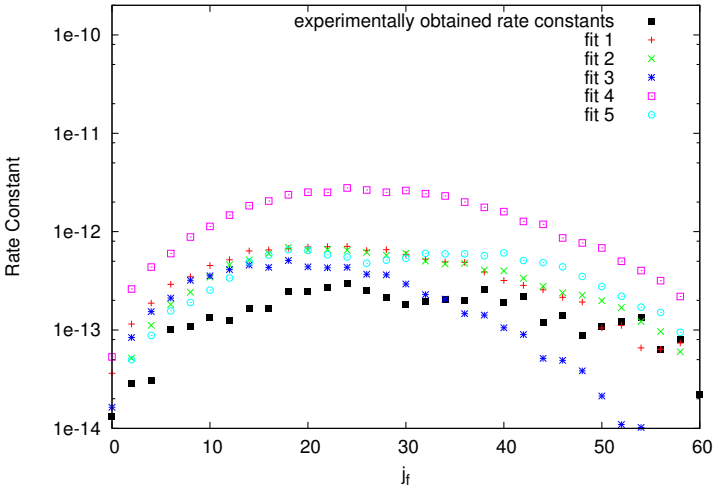

Figure 35: Fits of rovibrationally inelastic $v_i = 0, j_i = 18$ rate constant data with the breathing ellipsoid potential for $v_f = 1$.

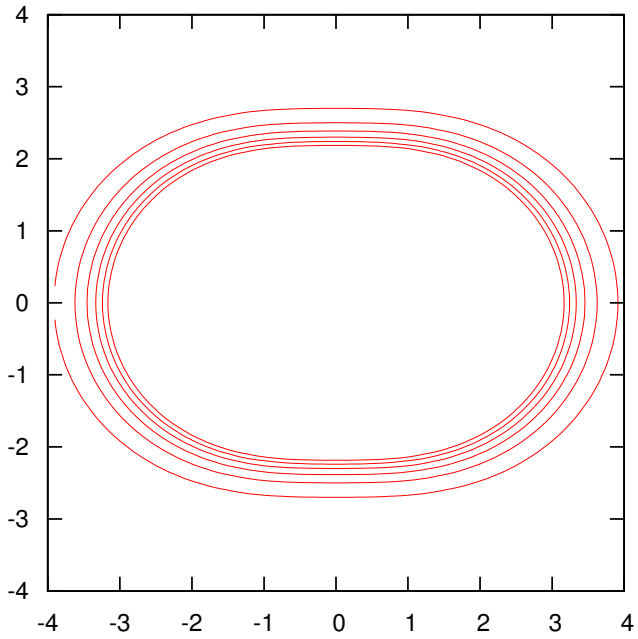

Figure 36: Contour plot for the potential that was the best of the fits from figures 34 and 35. The internuclear separation, r is fixed at $r = r_0$, and the contours are every 500 cm^{-1} from 500 to 3000 cm^{-1}.

Unfortunately, the fit of the vibrationally inelastic data is somewhat less successful. Certainly it is not good enough to extract potentials from lab data with the expectation of extracting a great deal of information from them. However, having reached a functional form that achieved reasonable fits to the data, we could attempt to modify the functional form somewhat with the hope of improving the fit by adding flexibility. This will be examined in section 7 of this chapter.

6. Fitting Data with Multiple v_i, j_i Values

Every previous three-body potential fit in this chapter used a set of data with a single set of v_i and j_i values. If there was a functional form that could create quality fits of all our data, such as the fit that the breathing ellipsoid can make to the rotationally inelastic data, it would make sense to simultaneously fit all the data for a given system. While the breathing ellipsoid potential does not create quality fits of all the data, it creates good enough ones of the rotationally inelastic data for it to be worth simultaneously fitting multiple sets of rotationally inelastic data.

In order to do this, we use $v_i = 2, j_i = 30$ experimental data (figure 37) [22,23]. The resulting fits are good, but there is room for improvement (figures 38 and 39). However, as was true in the case of the single data set vibrationally inelastic fits, the "breathing ellipsoid" potential needs to be modified in order to fit multiple data sets of vibrationally inelastic data.

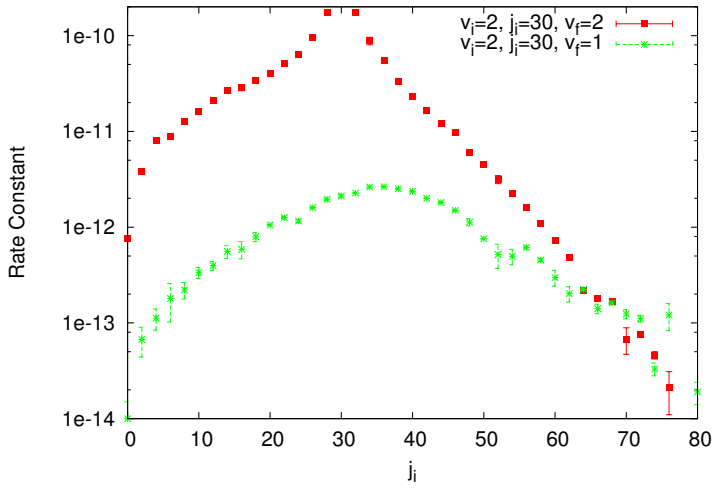

Figure 37: Experimental rate constants for $v_i = 2, j_i = 30$

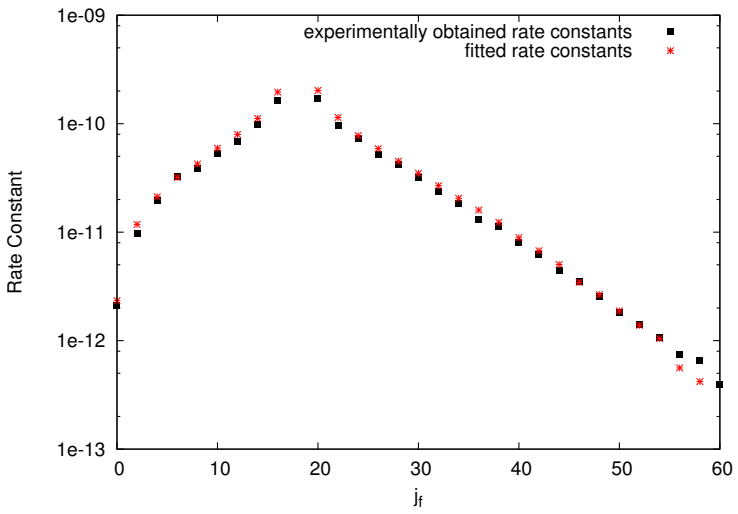

Figure 38: Breathing ellipsoid fit to data with multiple v_i, j_i values. Shown here is the $v_i = 0, j_i = 18$ part of the fit.

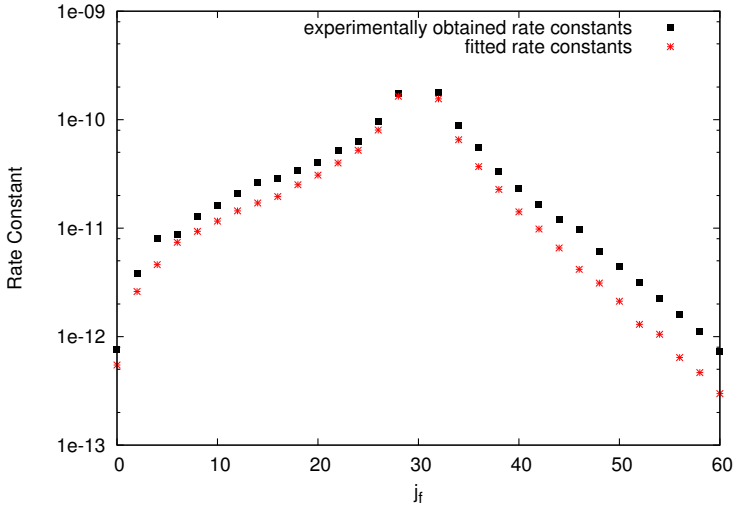

Figure 39: Breathing ellipsoid fit to data with multiple v_i, j_i values. Shown here is the $v_i = 2, j_i = 30$ part of the fit.

7. Direct Fitting to the *Ab Initio* Potential Surface

By directly fitting the *ab initio* potential, we can move rapidly gain an understanding for the success of a potential in fitting the *ab initio* potential. The degree of success in this task can be used to quickly judge potential functions as we search for one that contains the flexibility necessary to better model the data. In this section, we will show the improvement in the fit of one modification of the "breathing ellipsoid" potential function.

The "breathing ellipsoid" potential needed to be modified or abandoned in order to get a potential that could more reasonably fit the data. Theoretically, it is possible to modify new potential functions for our fitting routine and keep trying until we found one that fit the data sufficiently well.

It is much more efficient to fit directly to the existing *ab initio* potential we do have. While the *ab initio* potential is not an experimentally obtained result, as we discussed earlier, it is a very good approximation, such that finding a potential that can fit this potential more successfully than the simple "breathing ellipsoid" potential would be expected to improve the fit on the experimental line shape ratios. To set a baseline, we fit the "breathing ellipsoid" potential to the *ab initio* potential, getting a fit with $\chi^2/\nu = 0.4404$, fitting data ranging from close to 0 cm^{-1} to approximately 3000 cm^{-1}.

The Li_2 potential is known to decrease roughly exponentially with increasing R, but with much more complex dependence in γ than the "breathing ellipsoid" accommodates. To acco5modate that complex dependence in γ, we replace the second degree Legendre polynomials with a sum over even degree Legendre polynomials.

$$V = V_0 \exp\left(A - \frac{R - \alpha(r - r_0)[1 + a_1 P_2(\cos\gamma) + a_2 P_4(\cos\gamma) + a_3 P_6(\cos\gamma)]/c}{L/A\{1 + (a_1 P_2(\cos\gamma) + a_2 P_4(\cos\gamma) + a_3 P_6(\cos\gamma))[1 + \beta(r/r_0 - 1)]\}}\right) \tag{18}$$

where

$$c = 1 + a_1 + a_2 + a_3 \tag{19}$$

This fit is a significant improvement, with $\chi^2/\nu = 0.3571$. Still, this is not a good fit. To put this into perspective, a potential function that was identical to the *ab initio potential*, times 1.6, would have a $\chi^2/\nu = 0.3878$. Examining the data, the fits are not quite that bad: a large contribution to χ^2/ν comes from the potential being too high near the atoms in the molecule. Further, figures 28 and 33 suggest that we may need to do more to improve the potential: the added terms most strongly affect the anisotropy away from $r = r_0$, and even at equilibrium, the *ab initio* potential has a much more complex dependence on γ than do the fits from the "breathing ellipsoid" potential. To better fit the *ab initio* data and hopefully the experimental data as a result, we'll want to adjust our potential to better reflect fit the *ab initio* potential. By adjusting our potential function, we can find new forms that will hopefully be more successful in fitting vibrationally inelastic data and data with multiple v_i, j_i values.

CHAPTER 5

Conclusion

Having successfully developed a method for extracting velocity-dependent cross sections, the next step is to apply it. The level of success it meets in fitting experimental data will depend on the ability of the functional form of the cross section to fit the experimental cross section. The degree to which this function is able to do so and the fits that we find will be interesting.

It has not yet proven necessary, but it is also possible to pursue other functional forms. The strength of the current form is that it naturally models what we expect the experimental cross sections to be shaped like. If there are any that buck this trend or just are difficult to describe in terms of our potential form, other functional forms may be helpful

This is precisely what the three-body potential fitting needs. Although the breathing ellipsoid potential does a good job of fitting rotationally inelastic data, some modifications need to be made to more successfully fit vibrationally inelastic data and larger sets of data in general, including multiple v_i and j_i values in the data.

However, the work shown in chapter 4 is extremely encouraging. We have a functional form that can fit some of the data extremely well, and the anisotropy of the potential contour plot is certainly informative. Further work will be needed to see exactly how far this method can go.

Bibliography

[1] Marion, J. B., Thornton, S. T., *Classical Dynamics of Particles and Systems*, 4th Ed., 291-332, Saunders College Publishing (1995)

[2] Smith, R. H., Szebehely, V., Celestial Mechanics and Dynamical Astronomy, **56**, 409-425 (1993)

[3] Stewart, B. A., Stephens, T. N., Lawrence, B. A., McBane, G. C., J. Chem. Phys. A, **114**, 98759885 (2010)

[4] John C. Light, Bernstein, R. B., Ed., *Atom-Molecule Collision Theory*, 243-245, Plenum Press, New York (1979)

[5] Baumgartner, G., Kornmeier, H., Preuss, W. Chem. Phys. Lett. **107**, 1321 (1984)

[6] Alexander, M. H., Werner, H., J. Chem.Phys, **95**(9), 6524-6535 (1991)

[7] Schaefer III, H. F., Bernstein, R. B., Ed., *Atom-Molecule Collision Theory*, 45-46, Plenum Press, New York (1979)

[8] Moré, J. J., Lecture Notes in Mathematics, **630**105-116 (1978)

[9] Press, W. H., Teukolsky, S. A., Vetterling, W. T., Flannery, B. P., *Numerical Recipes in C*, 2nd Ed., 683-688, Cambridge University Press (1992)

[10] Butler, Ethan, Experimental Studies of Molecular Lithium Vapor, M.A. Thesis, Physics Department, Wesleyan (2005)

[11] Smith, N., T. Brunner, D. Pritchard, J. Chem. Phys., **74**(1), 467 (1981)

[12] Smith, N., Scott T., Pritchard D., J. Chem. Phys., **81**(3), 1229 (1984)

[13] Bernstein, R. B., *Atom-Molecule Collision Theory*, 29-34, Plenum Press, New York (1979)

[14] Matei, Paula; Personal Communication

[15] Coppage, Steve, Absolute Level-to-Level Rate Constants for Inelastic Collisions and Exchange Reactions in Li-$Li_2^*(v_i, j_i) \rightarrow Li_2^*(v', j')$−Li, Ph. D. Thesis, Physics Department, Wesleyan (2009).

[16] Gentry, W. R., Bernstein, R. B., Ed., *Atom-Molecule Collision Theory*, 394-396, Plenum Press, New York (1979)

[17] Pattengill, M. D., Bernstein, R. B., Ed., *Atom-Molecule Collision Theory*, 359-375, Plenum Press, New York (1979)

[18] M. Born and J. E. Mayer. Z. Physik , **75**, 118 (1932)

[19] M. Born and J. E. Mayer. J. Chem. Phys., **2** 252259 (1934)

[20] Magill, P. D., Stewart, B., Smith, N., Pritchard, D. E., Physical Review Letters **60**(19), 1943-1946 (1988)

[21] Gao, Y., Stewart, B., J. Chem. Phys. **103**, 860 (1995)

[22] Gao, Y., Gorgone, P. S., Davis, S., McCall, E. K., Stewart, B., J. Chem. Phys **104**(4), 1415-1426 (1996)